



Elastic modifications of an inertial instability in a 3D cross-slot

Konstantinos Zografas^{*,a}, Noa Burshtein^b, Amy Q. Shen^b, Simon J. Haward^b, Robert J. Poole^a

^a School of Engineering, University of Liverpool, Brownlow Street, Liverpool L69 3GH, UK

^b Okinawa Institute of Science and Technology Graduate University, Onna, Okinawa 904-0495, Japan



ARTICLE INFO

Keywords:

Spiral vortex
Cross-slot
Viscoelastic fluids
Inertial instability
Stagnation point

ABSTRACT

We numerically investigate inertial flows of viscoelastic fluids within a three-dimensional cross-slot geometry of square cross-section. Our study focuses on the inertial instability that occurs above a critical Reynolds number (Re) resulting in a transition to a steady flow asymmetry. We investigate numerically the effects of elasticity upon its characteristics by employing the upper-contracted Maxwell (UCM), the Oldroyd-B and the modified Chilcott-Rallison finitely extensible nonlinear elastic (FENE-MCR) models. In so doing, we show that the UCM and the Oldroyd-B model results are restricted to very low nominal Weissenberg numbers at non-negligible Reynolds numbers, due to a significant increase in the strain rate at the stagnation point caused by inertia. The resulting steady-asymmetric flow at these critical conditions gives rise to the formation of a single axially-aligned spiral vortex, which is formed along the outlet channels of the geometry in good agreement with experimental observations. Below these critical conditions the flow remains steady-symmetric, varying from a nearly two-dimensional flow at very low Re to a more complex three-dimensional flow at higher Re . In a recent publication [Burshtein et al. [Phys. Rev. X, 7, 041039, (2017)]], we demonstrated experimentally, accompanied by limited complementary numerical simulations, the impact of elasticity upon the critical conditions for which the instability develops and the behaviour of the subsequent growth of vorticity of the single spiral vortex. Our results here show how different viscoelastic models influence the instability in a 3D cross-slot and demonstrate an interesting behaviour of the first normal-stress difference, providing an additional insight on the potential mechanisms which are responsible for the suppression of the spiral-vortex. We also elucidate the role played by solvent-to-total viscosity ratio and the extensibility parameter in the FENE-MCR model on the instability.

1. Introduction

Cross-slot geometries have arguably increased their popularity among other extensional flow configurations, due to their ability to provide a range of different operations and for their inherent simplicity in terms of design and usage [1,2]. These types of geometries are composed of four intersecting channels with two opposing inlets and two opposing outlets. The two incoming fluid streams, with equal imposed flow rates, meet at the middle of the cross-slot and generate a free stagnation point, which is the hallmark of this configuration. The major characteristic of stagnation point flows, like the ones generated by cross-slots, is that fluid elements are either subjected to high velocity gradients for a limited time at the region surrounding the stagnation point, or are trapped at the stagnation point and are subjected to high strain rates for “infinite” time [2]. The importance of stagnation point flows for investigating different flow-type behaviours was initially recognized by Taylor, who introduced the four-roll mill design [3]. With this device, Taylor could generate strong extensional flows using a

matrix fluid and further deform or cause break-up of suspended droplets by trapping them at the stagnation point. Similar geometries and other set-ups able to generate extensional flows with free stagnation points such as opposed jet devices or cross-slots, were used for studying the dynamics of polymer molecules in extensional flows [4–7] or for investigating inertial instabilities [8–10]. More recently, microfluidic versions of stagnation point geometries (in particular cross-slots) have become popular [11–14]. Microfluidic devices typically operate at very low Reynolds numbers (i.e. creeping-flow conditions) such that Newtonian flow within a cross-slot geometry remains symmetric, thus providing a planar elongational field [2,15]. The low inertia also enhances the importance of elastic effects that arise due to microstructural deformations in complex fluids at high Weissenberg numbers. Furthermore, the planar nature of the cross-slots allows the response of complex fluids to the extensional flow field to be characterized and understood in details using experimental techniques such as flow velocimetry, birefringence measurement, and x-ray and neutron scattering [2].

* Corresponding author.

E-mail address: k.zografas@liv.ac.uk (K. Zografas).

Based on these characteristics, cross-slot geometries have found great success for investigating the generation of elastic instabilities in extensional flows of complex fluids, both experimentally [16–18], and numerically [19–23]. Their ability to apply large deformations around the stagnation point was exploited and has been employed to operate as possible extensional rheometers [2,15,24–26]. In particular, optimised shapes of the standard cross-slot were utilised to generate homogeneous extension at a well-defined region and not only in a small volume around the stagnation point, as occurs in the traditional set-up [14,27,28]. Moreover, microfluidic cross-slots have been used in biomedical research in order to trap and investigate the response of a single-molecule or of a single-cell of interest at the stagnation point, where their potential to serve as disease diagnostic platforms was reported [29–34].

The majority of studies related to microfluidic cross-slot geometries have investigated fluid flows and cell responses at very low Reynolds numbers (Re). However, a growing interest exists in inertial-microfluidics for cell-analysis and sample preparation [35,36] and also in strategies that can enhance mixing in microfluidics, to promote for example chemical reactions at moderate Re . As discussed in Oliveira et al. [37], mixing can be most easily achieved in turbulent flows, however flows in microfluidic components usually reside in the laminar regime and therefore this process of mixing is a challenging task using microdevices. Inducing inertial turbulence in microfluidic geometries is not easy and for many applications this can be undesired [38]. Other techniques which are based on molecular diffusion attempt to mix reactants at the microscale, but are not efficient due to the very small characteristic time scales. Therefore for passive micro-mixers, alternative solutions which exploit instabilities or fluid non-linearities have been proposed to enhance mixing [37].

In the early 1990s, Lagnado and Leal [8] investigated a Newtonian fluid flow within two four-roll mill devices designed with different aspect ratios. They demonstrated the generation of significant three-dimensional (3D) secondary flows as Re was increased from low to moderate values, leading to the onset of an inertial instability above a critical flow rate. Later, Kalashnikov and Tsiklauri [9,10] employed high aspect ratio (depth to width ratio) cross-slot channels and reported similar flow transitions in laminar flows of Newtonian fluids and polymer solutions of both low and high polymer concentrations. More importantly, the authors showed that although the inertial instability was not altered by the presence of the polymer additives, its quantitative characteristics were affected, illustrating a decrease in the critical Reynolds number (Re_c) for increasing elasticity number (El). Despite the fact that these flow transitions were known for similar flows, only recently the transitions for Newtonian fluids in a cross-slot were fully characterised by Haward et al. [39]. The authors investigated both experimentally and numerically the flow transition of a Newtonian fluid, from the steady-symmetric to the steady-asymmetric state, considering a range of microfluidic cross-slot devices that were fabricated with different aspect ratios. They demonstrated similar transitions as those presented by Lagnado and Leal [8] and reported the critical conditions for the onset of the inertial instability in terms of Re_c for each design. For low Reynolds numbers below Re_c ($Re \ll Re_c$), the flow remained steady-symmetric and could be considered as a nearly two-dimensional (2D) flow. When inertia was increased, but still remained below critical conditions ($Re < Re_c$), four symmetrically positioned Dean vortices were formed [40], with the flow still being symmetric relative to the flow centreplanes. For values above Re_c , a single spiral-vortex was formed and the flow was seen to undergo a bifurcation to a steady-asymmetric state. In this state, an axially-aligned spiral vortex extends along the outlet channels of the geometry. The authors performed both increasing and decreasing ramps of the imposed flow rate and characterised the flow bifurcation depending on the aspect ratio of the geometry. A similar type of inertial instability also occurs in T-shaped channels and was characterised by Poole et al. [41]. The ability of cross-slot and T-junction geometries to generate “vortex-flows” in

laminar conditions was exploited and the mixing performance with both configurations was investigated [42,43]. Recently, the heat transfer enhancement due to the spiral vortex instability in the cross-slot was investigated by Abed et al. [44], both experimentally and numerically. In their experiments, the authors used temperature-sensitive fluorescent dye and performed detailed measurements of temperature distributions. They were able to show an improved heat transfer between the two incoming fluid streams when the spiral vortex was formed and demonstrated a good agreement with their numerical simulations.

In our recent publication [45], we demonstrated in a series of experiments that the addition of small (order of a few parts-per-million, ppm) quantities of a flexible polymer to a Newtonian solvent, resulted in a great impact upon the critical conditions for which the instability in the cross-slot occurred. This was evident by the significant reduction in both Re_c and the subsequent growth of vorticity of the spiral vortex for all fluids considered. Our experimental studies were accompanied by limited complementary numerical simulations using the modified Chilcott-Rallison, FENE-MCR, model [46,47] and we demonstrated a near-quantitative agreement, providing an additional insight into how the instability mechanism is modified by the presence of fluid elasticity. Such significant elastic effects at such low polymer concentrations have usually only been reported in the context of turbulent drag reduction [48–51]. Thus the results also provide insights on possible mechanisms of drag-reduction and the observed vortex suppression by focusing only on a single stream-wise vortex.

Here we performed an extended series of 3D computational fluid dynamics (CFD) simulations in a cross-slot using the upper-convected Maxwell (UCM), the Oldroyd-B [52] and the FENE-MCR models [47]. We characterise the behaviour of these models for cases of constant elasticity numbers, trying to mimic real experiments, and report their behaviour for the cases of constant Weissenberg numbers but varying Re . For all cases the results are compared to the equivalent response of a Newtonian fluid. The numerical simulations provide a greater insight on the rich mechanisms of this inertial instability and on the flow destabilisation that occurs at lower Reynolds numbers when polymer solutions are employed compared to the Newtonian case.

The remainder of the paper is organised as follows. In Section 2 the governing equations and the theoretical models used are presented, followed by the overview of the numerical procedures and the material properties of the different models. In Section 3 the problem is described and the geometry employed is introduced together with the characteristic dimensionless numbers. Section 4 presents the numerical results obtained for the Newtonian fluid and the viscoelastic fluids considering two different approaches. Moreover, an investigation reporting the influence of the solvent-to-total viscosity ratio and the extensibility parameter is also provided. The section is concluded by demonstrating an interesting behaviour of the first normal-stress difference. Finally, the main conclusions of the current study are summarised in Section 5.

2. Governing equations

The critical conditions for which the inertial instability in the cross-slot occurs are investigated numerically using the UCM, Oldroyd-B and FENE-MCR models [47,52]. The flow for all fluids is considered to be laminar, incompressible and isothermal and is evaluated by performing 3D simulations using a finite-volume method [53]. The equations solved numerically are those of conservation of mass and momentum:

$$\nabla \cdot \mathbf{u} = 0, \quad (1)$$

$$\rho \left(\frac{\partial \mathbf{u}}{\partial t} + \mathbf{u} \cdot \nabla \mathbf{u} \right) = -\nabla p + \nabla \cdot \boldsymbol{\tau}, \quad (2)$$

where ρ is the density, p is the pressure, \mathbf{u} is the velocity vector, and $\boldsymbol{\tau}$ is the stress tensor consisted of the polymeric, τ_p , and solvent, τ_s , components ($\boldsymbol{\tau} = \tau_s + \tau_p$). The contributions of the solvent component to the

stress tensor are expressed by the Newtonian constitutive equation $\tau_s = \eta_s(\nabla\mathbf{u} + \nabla\mathbf{u}^T)$, with η_s being the solvent viscosity. In order to account for the effects of elasticity, the polymeric part of the stress tensor is described by an appropriate constitutive equation. Here all models are compactly described by the equation of the FENE–MCR model, of which the UCM and the Oldroyd-B models are limiting cases:

$$\tau_p + \frac{\lambda}{g(\tau_p)} \overset{\circ}{\tau}_p = \eta_p(\nabla\mathbf{u} + \nabla\mathbf{u}^T). \quad (3)$$

In Eq. (3), $\overset{\circ}{\tau}_p$ is the upper-convected derivative of the polymeric component of the stress tensor, λ is the relaxation time and η_p is the polymeric contribution to the total viscosity. The ratio, $\beta = \eta_s/\eta$, between the solvent viscosity (η_s) and the total shear viscosity of the investigated fluid ($\eta = \eta_s + \eta_p$) is called the solvent-to-total viscosity ratio. The function $g(\tau_p)$ of the stress tensor in Eq. (3) is defined as

$$g(\tau_p) = \frac{L^2 + (\lambda/\eta_p)\text{Tr}(\tau_p)}{L^2 - 3}, \quad (4)$$

where L^2 is the extensibility parameter and $\text{Tr}(\tau_p)$ corresponds to the trace operator of the polymeric stress tensor. The extensibility parameter is used to relate the maximum length of a fully-extended dumbbell to its equilibrium length and here is set as $L^2 = 5000$, unless stated otherwise, in order to match the experimental conditions of the polymer solutions with constant viscosity employed in our previous study [45]. At the limiting case of $L^2 \rightarrow \infty$, Eq. (3) reduces to the Oldroyd-B model, while for $L^2 \rightarrow \infty$ and $\eta_s = 0$ the UCM model is recovered.

All three viscoelastic models considered exhibit constant shear viscosity, with the UCM and the Oldroyd-B models predicting a constant first normal-stress coefficient. On the contrary, the FENE–MCR model predicts a non-zero but shear-thinning first normal-stress coefficient which is controlled by the value of L^2 [47].

Free stagnation point flows like the ones generated by a cross-slot configuration provide the appropriate conditions which achieve steady extension [2,28]. It is well known that under these conditions the UCM and the Oldroyd-B models will predict an infinite extensional viscosity, η_e , above a critical local Weissenberg number $Wi_{\dot{\varepsilon}} = \lambda\dot{\varepsilon} = 0.5$ [19,52,54], where $\dot{\varepsilon}$ is the applied strain rate. Although solutions obtained from CFD simulations above this critical value are sometimes possible due to the integrable stress field, their influence on the inertial instability in such cases is clearly unphysical [55] and therefore, we decided to limit the use of these two models by estimating the local $Wi_{\dot{\varepsilon}}$ at the stagnation point as will be discussed in detail later. On the other hand, all FENE models, and therefore the FENE–MCR model employed here, exhibit a more realistic behaviour by predicting a bounded response for η_e [47,54,56,57] and thus its usage can be extended to $Wi_{\dot{\varepsilon}} > 0.5$. This behaviour of the extensional viscosity, non-dimensionless here by η , is shown in Fig. 1a considering steady planar extension, where the response of the Oldroyd-B model for $\beta = 0.90$ is compared to the predictions of the FENE–MCR model for $\beta = 0.90$ under different values of the L^2 parameter and for $\beta = 0.95$ with $L^2 = 5000$. Additionally, in Fig. 1b the dimensionless first normal-stress difference, $N_1/2\tau = (\tau_{xx} - \tau_{yy})/2\tau$, for steady shear flows of the same cases is shown, where τ corresponds to the applied shear stress. For the Oldroyd-B and UCM models, the growth of the dimensionless first normal-stress difference is unbounded, increasing linearly with $\lambda\dot{\gamma}$, where $\dot{\gamma}$ is the applied shear rate, since it can be shown that $N_1/2\tau = (1 - \beta)\lambda\dot{\gamma}$. For the FENE–MCR model it can be shown that when $\lambda\dot{\gamma} > > 1$, the first normal-stress difference is bounded, reaching to a plateau at $N_1/2\tau \sim (1 - \beta)((L^2 - 3)/2)^{1/2}$.

The set of the governing equations (Eqs. (1)–(4)) are solved numerically using an in-house implicit, time marching, finite volume CFD solver, appropriate for collocated numerical grids, described in detail in Oliveira et al. [58] and Oliveira [59]. The convective terms in both the momentum equation (Eq. (2)) and the stress constitutive relation

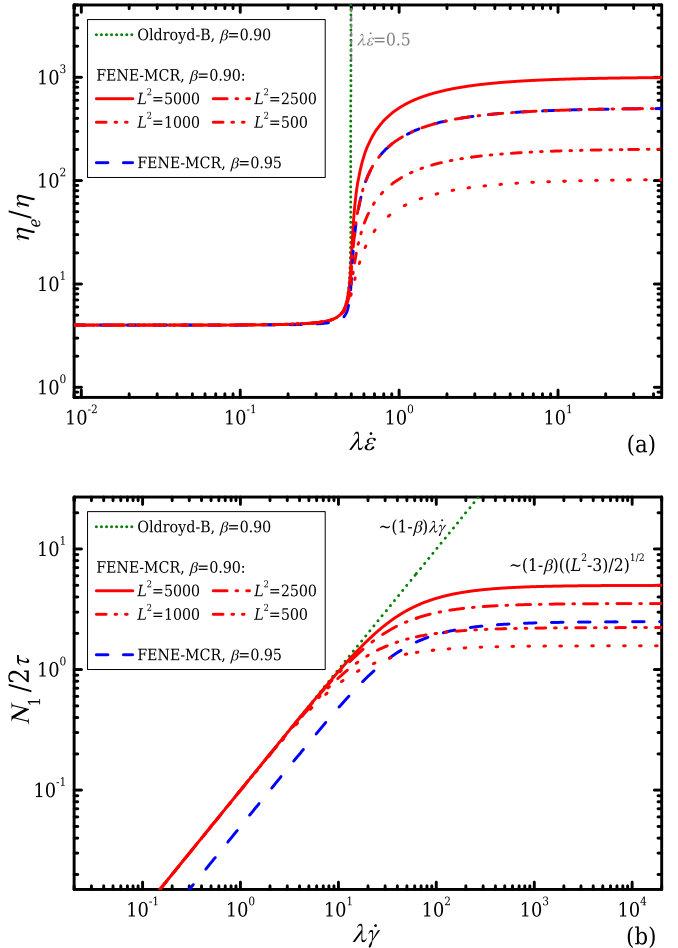


Fig. 1. Viscometric properties of the Oldroyd-B model for $\beta = 0.90$, the FENE–MCR model for $\beta = 0.90$ using different values of L^2 , and the FENE–MCR model with $L^2 = 5000$ for $\beta = 0.95$. (a) Extensional viscosity in steady extensional planar flow scaled by the total shear viscosity, and (b) first normal-stress differences scaled by the characteristic total shear stress ($\tau = \eta\dot{\gamma}$) in steady shear flows.

(Eq. (3)) are discretised with the CUBISTA high-resolution scheme proposed by Alves et al. [60]. The diffusive terms are discretised considering a central difference scheme, while the transient terms are evaluated using a first-order implicit Euler scheme. It is noted here that, since we are interested only in the steady-state solutions (steady-state instability), the first-order of accuracy is not restrictive due to the vanishing time derivative when steady-state is reached.

Finally, a useful parameter that is employed in order to discuss our results in Section 4.5 is the flow-type parameter defined as

$$\xi = \frac{\|\mathbf{D}\| - \|\boldsymbol{\Omega}\|}{\|\mathbf{D}\| + \|\boldsymbol{\Omega}\|}, \quad (5)$$

where $\|\mathbf{D}\| = \left(\frac{D:D}{2}\right)^{1/2}$ is the magnitude of the rate-of-deformation tensor, $\mathbf{D} = \frac{1}{2}[\nabla\mathbf{u} + (\nabla\mathbf{u})^T]$, and $\|\boldsymbol{\Omega}\| = \left(\frac{\boldsymbol{\Omega}:\boldsymbol{\Omega}}{2}\right)^{1/2}$ is the magnitude of the vorticity tensor, $\boldsymbol{\Omega} = \frac{1}{2}[\nabla\mathbf{u} - (\nabla\mathbf{u})^T]$. Using the velocity field from the CFD simulations, the ξ parameter is evaluated and varies within the range $[-1, 1]$. When $\xi = -1$ the flow is rotational, when $\xi = 1$ the flow is characterised by pure extension and when $\xi = 0$ the flow is simple shear [4,61].

3. Problem description and dimensionless numbers

The three-dimensional cross-slot geometry used in this study is illustrated in Fig. 2. The fluid of interest is injected from the two

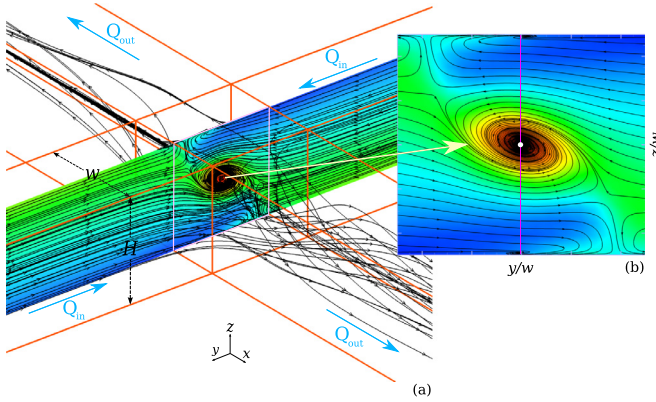


Fig. 2. (a) Cross-slot configuration with $AR = H/w = 1$. (b) Interrogation region where the dimensionless centrepoint vorticity, ψ , is evaluated in order to report the critical conditions of the formation of the spiral vortex. Streamlines of yz -centreplane are projected on the corresponding contours of the axial vorticity $\omega_x = (\partial u_z / \partial y) - (\partial u_y / \partial z)$ for a Newtonian fluid.

opposing inlets with equal flow rates along the y -direction and is directed along the x -direction to the exits of the two opposing outlets. In our simulations, fully-developed velocity profiles are imposed at the inlets of the cross-slot and zero stream-wise gradients are considered for the velocities and the stresses at the outlets. The width, w , of the device is set to be equal to the height, H , resulting a geometry with an aspect ratio $AR = H/w = 1$.

As was shown in Haward et al. [39], the inertial instability of Newtonian fluids in cross-slot configurations may be generated when a critical Reynolds number is exceeded. The Reynolds number is defined as

$$Re = \frac{\rho U w}{\eta}, \quad (6)$$

where U is the mean inlet velocity. When performing ramps of increasing Re the flow initially remains steady-symmetric at low values. As the flow rate is gradually increased it reaches to a critical point (Re_c) where it is then replaced by a steady-asymmetric flow [8,39]. The opposite transition occurs for decreasing ramps from above the critical flow rate, which we use here to report the critical conditions. Starting from an already steady-asymmetric case, we seek the steady solution of the flow field at smaller flow rates and the critical Reynolds number, Re_c^* , below which the flow returns to a steady-symmetric state. Hysteresis in the critical value between the increasing and decreasing ramps may or may not occur depending on the aspect ratio of the cross-slot device AR [39]. For the particular case investigated here with $AR = 1$, hysteresis in the transition is expected [39,45] at least for a Newtonian fluid. The single axially-aligned spiral vortex that is formed during the flow destabilisation is shown in Fig. 2, and extends for a length along the outlet channels of the geometry remaining steady in time (see Fig. 2a), at least until significantly larger Reynolds numbers are reached. It is mentioned here that although in the current study we focus on the steady-state inertial instability, it was shown experimentally in Burshtein et al. [45] that as the polymer concentration of the fluid is increased, the flow becomes unsteady, with the position and the magnitude of the vorticity fluctuating in time.

For all fluids considered in this study, the results are reported using an instability parameter, the dimensionless centrepoint vorticity ψ , evaluated at the geometric centre of the cross-slot as shown in Fig. 2b. The instability parameter is evaluated from the axial component (x -direction) of vorticity, $\omega_x = (\partial u_z / \partial y) - (\partial u_y / \partial z)$, using the numerical solution obtained for the velocity field and is non-dimensionalised as

$$\psi = \frac{w}{U} \omega_{x(y=z=0)}. \quad (7)$$

When viscoelastic fluid flows are investigated in order to

characterise the effects of viscoelasticity, a Weissenberg number is needed [62,63] to provide a measure of the ratio of elastic to viscous forces. Here the Weissenberg number is defined as $Wi = \lambda U / w$. However, due to the variety of the fluids we examine (with or without solvents) and in order to take into account the solvent contributions to the above definition, we also define an “effective” Weissenberg number as an additional parameter:

$$Wi_{eff} = (1 - \beta) Wi. \quad (8)$$

This definition takes into account that the solvent viscosity contributes to the viscous stresses but not the elastic stresses. Concluding, an indication of the balance between the elastic to viscous forces is provided by the elasticity number El , defined here as

$$El = \frac{Wi_{eff}}{Re} = (1 - \beta) \frac{\lambda \eta}{\rho w^2}, \quad (9)$$

which is independent of the kinematics and depends only on the geometric and fluid properties (in the absence of shear-thinning).

4. Numerical results and discussion

In this section we report our results from the 3D simulations, which follow two different strategies. Before explaining the results from these strategies, all behaviours of the viscoelastic fluids are presented in comparison to the equivalent Newtonian response which is used as a reference. Therefore, initially we demonstrate our results just for the Newtonian case and compare them to existing results in literature [39,44]. Then, for the first strategy, and in order to closely reproduce real flow conditions, a number of simulations are performed considering that El remains fixed (cf. Eq. (9)). For these particular cases, ramps are performed both up and down in Re in order to examine the value of Re_c for which the onset of the instability occurs and the value Re_c^* below which the instability vanishes. For the second approach, all evaluations start from an initially steady-asymmetric solution and then the Reynolds number is progressively reduced while Wi is kept constant (thus the fluid elasticity number changes). The critical Reynolds number Re_c^* , below which the flow returns to steady symmetric is reported.

4.1. Newtonian fluid behaviour and implications for singular models (UCM and Oldroyd-B)

Fig. 3 illustrates the transition from steady-asymmetric to steady-symmetric flow, while performing decreasing ramps of Re from an initially high value ($Re = 50$). The superimposed streamlines on top of the contours of the evaluated dimensionless vorticity depict the single steady spiral-vortex formed for $Re = 50$ (cf. Fig. 3a). As Re is decreased the flow reaches to the critical value of $Re_c^* \sim 40$ where the intensity of the vortex decreases and the dimensionless centrepoint vorticity obtains its minimum non-zero value (cf. Fig. 3b). Further decreases of Re result in a flow that is steady-symmetric relative to the flow centreplanes, with viscous forces managing to damp any disturbances. As can be seen in Fig. 3c for the case of $Re = 39$, the four counter-rotating symmetrically positioned Dean vortices [40] are formed, as was shown in Haward et al. [39], with the non-dimensional centrepoint vorticity obtaining a zero value ($\psi = 0$). For lower Reynolds numbers the Dean vortices vanish and the flow can be considered quasi 2D when $Re < 5$ (except close to the walls).

In Fig. 4a, the behaviour of the non-dimensional centrepoint vorticity for a Newtonian fluid is presented for both increasing and decreasing Re ramps. It can be seen that a hysteresis exists at the critical conditions for the inertial instability between the two ramps considered, similar to what was found numerically in Haward et al. [39] and also experimentally in Burshtein et al. [45] when using a cross-slot geometry with $AR = 1$. Here, the critical Reynolds for the decreasing

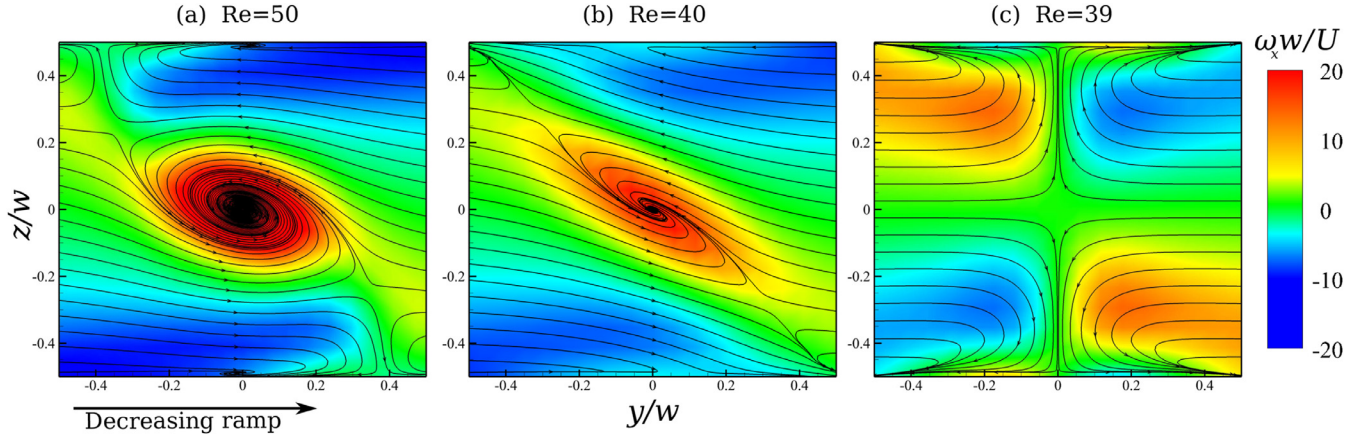


Fig. 3. Dimensionless vorticity contours with superimposed streamlines in the interrogation area for decreasing ramps of a Newtonian fluid.

ramps is found to be at $Re_c^* \sim 40$, while for the increasing ramps the onset of the instability is at $Re_c \sim 46$, with both values being in good agreement with the study of Haward et al. [39]. It is pointed out here that the hysteresis observed in our numerical simulations for Newtonian fluids (and, as will be shown later, also for viscoelastic fluids) depends on the level of noise and therefore on many factors (i.e. numerical solver, numerical method, mesh size). For example, in Abed et al. [44], the authors used the finite-volume method within ANSYS workbench and they reported the onset of the inertial instability for increasing ramps at $Re_c \sim 53$. On the other hand, the critical Reynolds number, Re_c^* where the transition occurs for decreasing ramps is found to be more repeatable. Both in Haward et al. [39] and in Abed et al. [44], it is reported at $Re_c^* \sim 40$. More importantly, in Burshtein et al. [45] we demonstrated a near quantitative agreement between experiments and numerical simulations for the obtained Re_c^* with decreasing ramps for Newtonian and viscoelastic fluids. Thus, in the remainder of the paper for all the fluids considered in this study, we report the values of Re_c^* obtained from the decreasing ramps.

Concluding with the Newtonian case and before discussing the behaviour of the viscoelastic fluids, we use the results obtained here to capture the development of the strain rate along $y = 0$ on the xy -centreplane at the stagnation point, evaluated as $\dot{\varepsilon} = \partial u_y / \partial y$. As mentioned earlier in Section 2, the values of $\dot{\varepsilon}$ limit the cases that can be examined when the UCM and the Oldroyd-B models are employed. This is due to the infinite values of the extensional viscosity predicted by these models beyond $\lambda\dot{\varepsilon} = 0.5$ in any steady-state extensional flow, as occurs at the geometric centrepoint in our cross-slot due to infinite residence time ($u_x = u_y = 0$). Fig. 4b demonstrates the corresponding dimensionless strain rate obtained from the non-dimensional streamwise velocity along the flow centreline, for the cases of decreasing Re . For creeping-flow conditions ($Re \rightarrow 0$) the strain

rate has its maximum absolute value with $|\dot{\varepsilon}/(w/U)| \sim 4$ as expected; i.e. assuming the velocity varies from $\sim +2U$ to $\sim -2U$ over a distance w . At the critical value $Re_c^* = 40$, where the spiral vortex is formed, the applied strain rate at the stagnation point reaches its maximum value with $|\dot{\varepsilon}/(w/U)| \sim 7.5$. Interestingly, for $Re > 40$ the absolute strain rate at the stagnation point obtains smaller values, with the centrepoint strain-rate exhibiting a non-monotonic behaviour with Re . Using the maximum obtained value at $Re = 40$ and evaluating the critical local Weissenberg number based on the elongation rate at the stagnation point ($Wi_{\dot{\varepsilon}} = \lambda\dot{\varepsilon}$), it can be determined that the limiting values for the UCM and the Oldroyd-B fluids are at a nominal $Wi \sim 0.0667$ and therefore for the Oldroyd-B at potentially negligible Wi_{eff} value (i.e. for $\beta = 0.95$ at $Wi = 0.0667$, $Wi_{eff} = 0.003335$; see Eq. (8)). This shows that in 3D cross-slots with inertia, the UCM and the Oldroyd-B models are restricted to vanishingly small effective Weissenberg numbers.

4.2. Constant elasticity number cases

Several viscoelastic fluids were investigated under conditions of constant elasticity number (cf. Eq. (9)). Fig. 5a demonstrates the behaviour of the UCM and the FENE-MCR models with $\beta = 0$ for $El = 0.00083$. In Fig. 5b the behaviour predicted for the FENE-MCR model with $\beta = 0.90$ and $\beta = 0.97$ at $El = 0.0042$ and $El = 0.00083$ respectively is shown, and in Fig. 5c the equivalent response for the FENE-MCR model with $\beta = 0.95$ at $El = 0.0021$ and $\beta = 0.99$ at $El = 0.00018$ is presented. For all cases considered, irrespectively of whether the ramps are increasing or decreasing, both Re_c and Re_c^* are reduced compared to the response of the Newtonian fluid. Additionally, similar to the case of the Newtonian fluid, all viscoelastic fluids exhibit a hysteretic behaviour in the critical conditions.

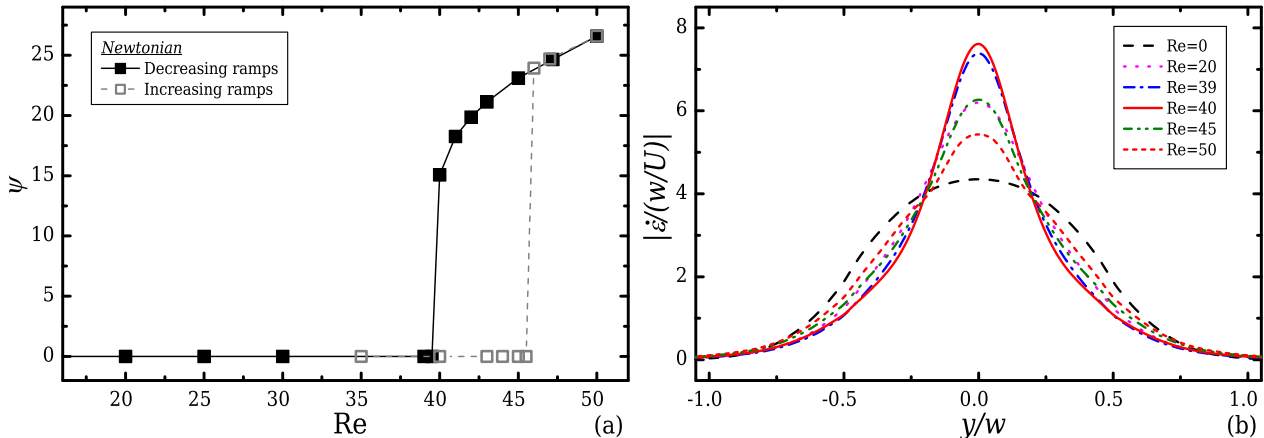


Fig. 4. (a) Behaviour of the dimensionless centrepoint vorticity for a Newtonian fluid and (b) dimensionless absolute streamwise strain rate ($\dot{\varepsilon} = \partial u_y / \partial y$) along the inlet flow centreline obtained for decreasing ramps of Reynolds numbers.

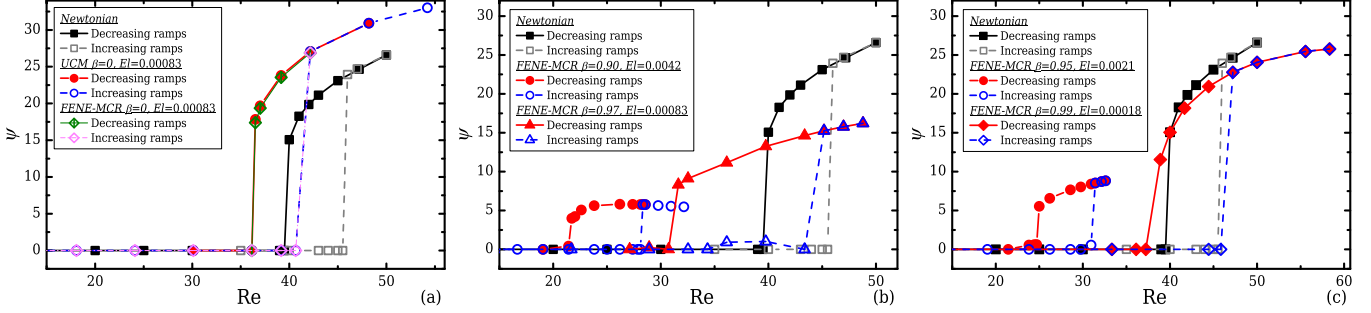


Fig. 5. Behaviour of the dimensionless centrepoint vorticity for the (a) UCM and FENE–MCR with $L^2 = 5000$ for $\beta = 0$ at $El = 0.00083$, (b) FENE–MCR with $L^2 = 5000$ for $\beta = 0.90$ at $El = 0.0042$ and $\beta = 0.97$ at $El = 0.00083$ and (c) FENE–MCR with $L^2 = 5000$ for $\beta = 0.95$ at $El = 0.0021$ and $\beta = 0.99$ at $El = 0.00018$ when increasing and decreasing ramps are performed in comparison with the equivalent behaviour of the Newtonian fluid.

Examining the behaviour of the centrepoint vorticity, it can be seen that, depending on the elasticity and the choice of β , the viscoelastic fluids demonstrate different behaviours when the flow is steady-asymmetric. For the UCM fluid and the equivalent FENE–MCR fluid with $\beta = 0$, that do not contain any solvent contributions (cf. Fig. 5a), almost identical solutions are obtained, with ψ following a solution branch at higher values compared to the Newtonian case at the investigated low elasticity values. On the other hand for all the remaining FENE–MCR fluids that are characterised by small amounts of polymer contributions, it is observed that as β decreases, the vorticity growth also decreases with Re while $Re \geq Re^*$. The latter is in line with the experiments performed for solutions of small quantities of a flexible polymer in Newtonian solvents [45]. As we have recently shown in Burshtein et al. [45], the complementary numerical simulations we performed demonstrate a near-quantitative agreement with experiments. However, as seen from the response of the viscoelastic fluids in Fig. 5a for low β values the resulting behaviour is a spiral vortex with higher centrepoint vorticity compared to the Newtonian case. This increase of the centerpoint vorticity at this low elasticity regime depends on the choice of β , and this behaviour has not yet been observed experimentally. Considering that the fluids described by the FENE–MCR model, shown in Fig. 5b and 5c, are characterised by small polymer concentrations, it can be realised that the level of influence of the polymer to the flow and the modifications observed are remarkable. Such significant elastic effects with very low polymer concentrations have usually only been reported in the context of turbulent drag reduction [48–51].

In Fig. 6 the contours of the dimensionless vorticity and the streamlines at the interrogation area are shown, depicting the form of the steady-state spiral vortex which is obtained from the simulations for the UCM model at $El = 0.00083$ and the FENE–MCR fluids for $\beta = 0.90$ and $\beta = 0.95$ at $El = 0.0042$ and $El = 0.0021$, respectively. It is noted here that the clockwise or the anticlockwise orientation of the spiral vortex occurs with the same probability for all cases [39], thus the bifurcation is perfect. Although

for consistency we show the same direction of rotation in all the plots included here.

The numerical solutions for the decreasing ramps obtained for the UCM model at $El = 0.00083$ and the FENE–MCR model with $\beta = 0.95$ at $El = 0.0021$ using our base mesh consisting of 63,291 numerical cells, were repeated with a more refined mesh consisting of 203,125 numerical cells in order to verify the mesh-dependency of our numerical simulations. Minor deviations with a maximum variation of 4% on the critical Reynolds number obtained between meshes were found. Therefore, the remaining results presented here were obtained using the less refined base-mesh.

4.3. Constant Weissenberg number cases

Here the behaviour of the viscoelastic fluids following our second strategy is presented. During this procedure the Weissenberg number remains constant, while only decreasing ramps of Re are performed until Re_c^* is encountered. Fig. 7 demonstrates the behaviour of the FENE–MCR fluids with $\beta = 0.90$ and $\beta = 0.95$ and the behaviour of the Oldroyd-B fluids with $\beta = 0.50$, $\beta = 0.75$ and $\beta = 0.95$ compared with the FENE–MCR model for $L^2 = 5000$ under the same conditions (β and Wi). For all cases, the Newtonian behaviour is also included for comparison. Particularly for the Oldroyd-B fluids, only the investigated cases at $Wi = 0.05$ (which are below the restricting Weissenberg number) are shown, and are compared with the equivalent response from the FENE–MCR model.

As in the cases of constant elasticity number presented previously, the flow transition for all fluids at all investigated Wi_{eff} occurs at a Reynolds value which is found to be smaller than the equivalent critical value of Newtonian fluids. For moderate Wi_{eff} , the FENE–MCR fluids (Fig. 7a and 7b) preserve the inertial instability with reduced centrepoint vorticity values, as was seen in Section 4.2 for the constant elasticity cases. We believe that this behaviour is closely related to the already known mechanism from studies related to turbulent drag reduction. As discussed in

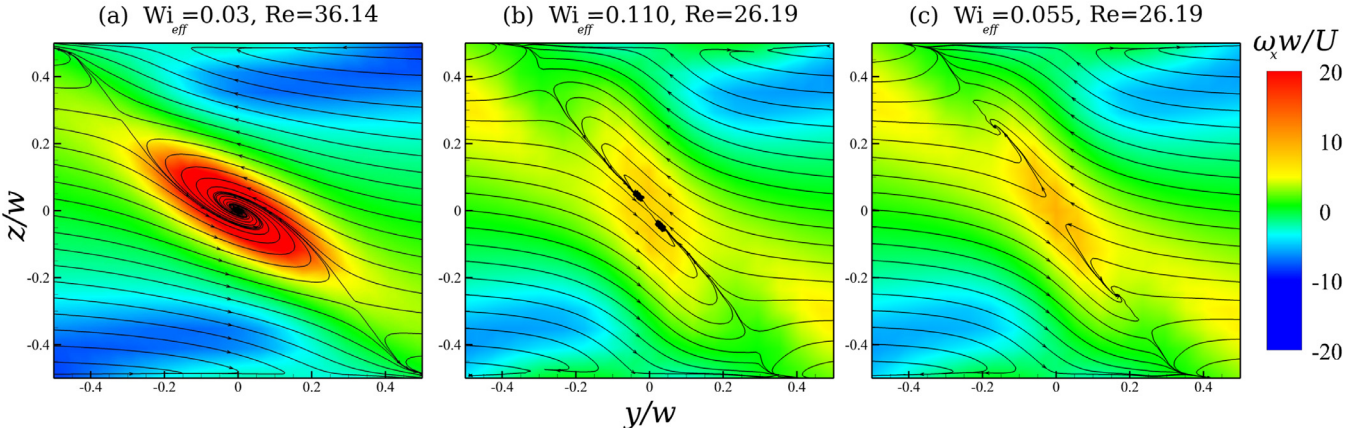


Fig. 6. Dimensionless vorticity contours with superimposed streamlines in the interrogation area for decreasing ramps for the (a) UCM at $El = 0.00083$, (b) FENE–MCR with $L^2 = 5000$ for $\beta = 0.90$ at $El = 0.0042$, and (c) FENE–MCR with $L^2 = 5000$ for $\beta = 0.95$ at $El = 0.0021$.

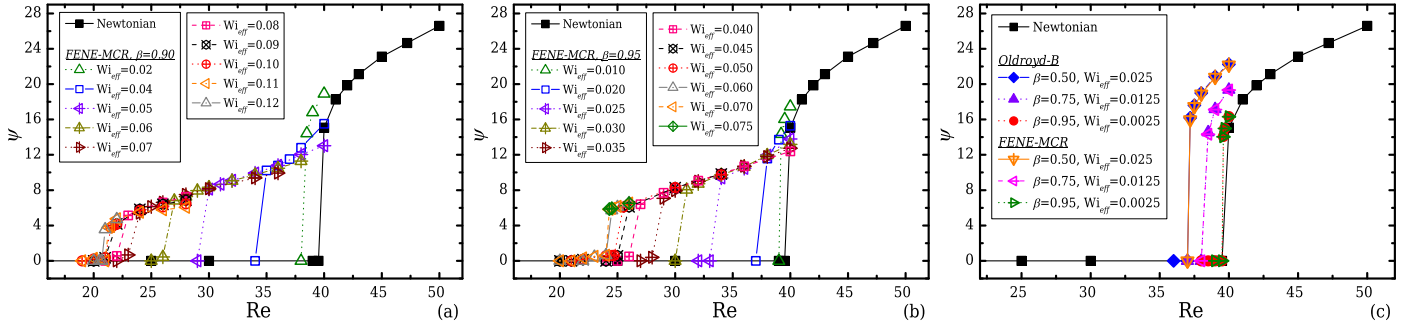


Fig. 7. Behaviour of the FENE-MCR fluids with $L^2 = 5000$ when (a) $\beta = 0.90$ and (b) $\beta = 0.95$, at decreasing Re ramps while Wi is constant and (c) behaviour of the Oldroyd-B and the equivalent FENE-MCR with fluids with $L^2 = 5000$ and $\beta = 0.50$, $\beta = 0.75$ and $\beta = 0.95$ at Re decreasing ramps when $Wi = 0.05$. All cases are compared to the response of the Newtonian fluid.

Kim et al. [49], the torque generated by the polymer forces opposes the rotation of the vortices, randomly created in the turbulent flow, decreasing their vorticity. Here it is restricted to a single vortex that is formed in a very controlled manner. On the contrary, for the low $Wi_{eff} \lesssim 0.025$ fluids shown in Fig. 7 (FENE-MCR and Oldroyd-B models), it can be seen that although the critical conditions are found to occur for lower Re , the centrepoin vorticity obtains higher values than the equivalent of the Newtonian case. This trend is similar to what was observed in the cases of constant elasticity. Moreover, the response of the Oldroyd-B model shown in Fig. 7c demonstrates clearly that this effect depends on the choice of β (Wi is the same for all fluids), with these results being accurately reproduced by the FENE-MCR model.

In Fig. 8 both the Weissenberg and the effective Weissenberg number (cf. Eq. (8)) are plotted as a function of Re_c^* , for all viscoelastic fluids investigated. Together with the results obtained from the constant Weissenberg number cases, which are presented with open symbols, also the cases discussed previously in Section 4.2 of constant El are included and indicated with closed symbols. More specifically in Fig. 8a it can be seen that as the elastic forces and the polymer concentration are increased ($c \equiv \eta_p/\eta_s = (1/\beta) - 1$, [56]) for the FENE-MCR model, the critical conditions of the transition are shifted towards lower Reynolds number values compared to the Newtonian case. The same also applies for the UCM and the Oldroyd-B models, for which our investigation is limited by the critical Weissenberg number at the stagnation point ($Wi_e = 0.5$) and is only applicable for very small elasticity values. It can be seen that they exhibit a behaviour similar to that seen for the FENE-MCR model, with the critical conditions for the onset of the inertial instability encountered at lower values of Re .

Taking into account the solvent contributions, in Fig. 8b two regions can be identified. For the first one, region (I), which corresponds to the flow stages ($Re_c^* \gtrsim 36$) where the elasticity of the fluids remains at low

values, it can be seen that the data corresponding to the critical conditions of the transition collapse in a similar trend. However, as can be seen from region (II) and while elasticity is increased, the polymer contributions become more dominant and affect the resulting flow field more. For these cases, the fluids demonstrate a slightly different response which is influenced by the different concentrations considered. Thus in region (I) and the limit $(Re_c^{*,N} - Re_c^*)/Re_c^{*,N} \ll 1$, where $Re_c^{*,N} \sim 40$ is the critical Reynolds number for a Newtonian fluid, Wi_{eff} is sufficient to collapse the data. However, further away from this limit, some β -dependency remains.

4.4. Effects of viscosity ratio and extensibility

Here we investigate the effects of the β and L^2 parameters upon the formation of the inertial instability using the FENE-MCR model. In Fig. 9 the influence of the solvent-to-total viscosity ratio β on the characteristics of the instability for a fixed extensibility parameter $L^2 = 5000$ and for a constant low Weissenberg number $Wi = 0.05$ is shown. More specifically, it can be seen in Fig. 9a that when the viscosity ratio is small and thus, the fluid is dominated by the polymeric contributions, the dimensionless centerpoint vorticity obtains higher values as compared to the Newtonian fluid. As the fluid becomes less elastic (decreasing Wi_{eff}) and therefore is mostly controlled by the solvent part, the dimensionless vorticity at the geometric centerpoint is approaching the Newtonian limit. These results verify further our initial observations with the UCM model (c.f. Section 4.2) and those with the Oldroyd-B model, demonstrating a strong dependency on the choice of β . In Fig. 9b the variation of ψ as a function of β for different Reynolds numbers is presented. It can be seen that for the more elastic fluids ($\beta \leq 0.25$), ψ decreases linearly with increasing β . Additionally, in the same figure the variation of the critical Reynolds number Re_c^* for each

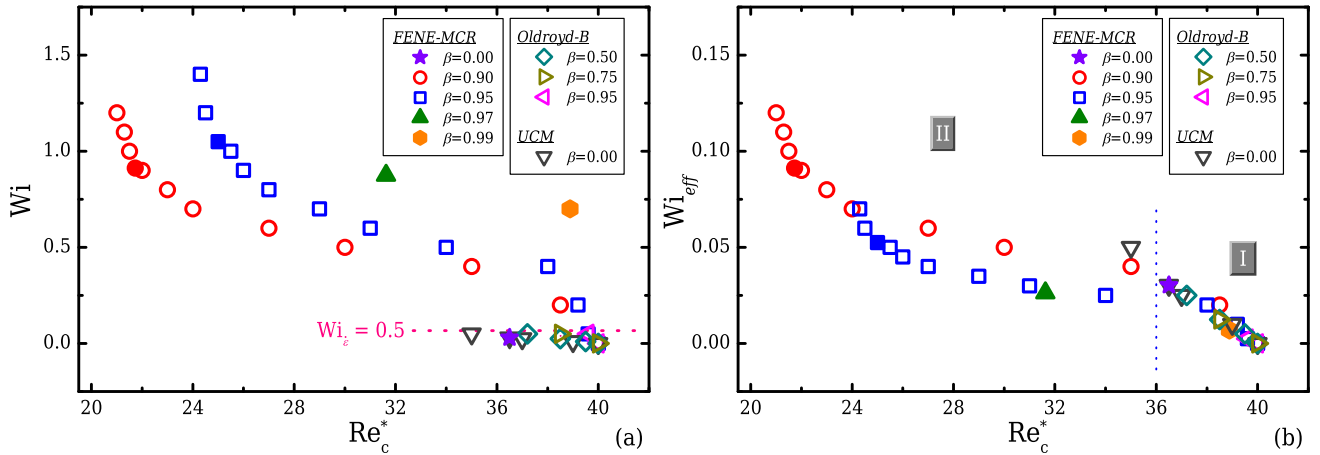


Fig. 8. (a) Weissenberg number and (b) effective Weissenberg number as a function of Re_c^* for all viscoelastic fluids considered in this study. The closed symbols correspond to the cases where El is maintained constant, while the open symbols refer to the cases of constant Wi .

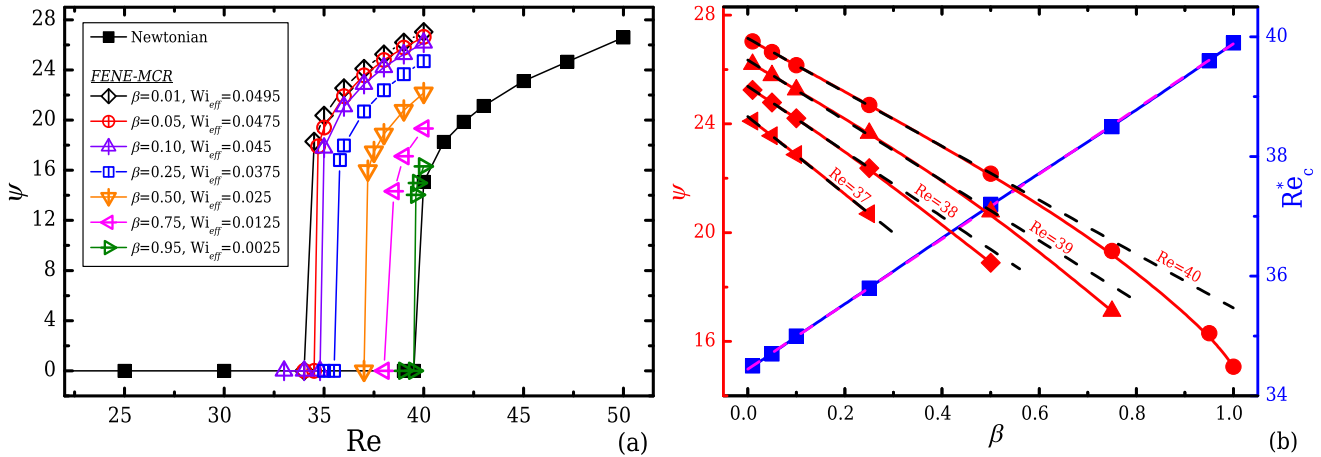


Fig. 9. (a) Behaviour of the FENE–MCR fluids for a range of viscosity ratios ($0.01 \leq \beta \leq 0.95$) when $L^2 = 5000$ at decreasing Re ramps while $Wi = 0.05$, in comparison to the response of the Newtonian fluid. (b) Variation with β of the dimensionless centerpoint vorticity at different Re and of Re_c^* . The solid lines are a guide to the eye while the dashed lines are a linear fit of the points for $\beta \leq 0.25$ for Ψ and of all points for Re_c^* .

fluid is shown, clearly demonstrating that by increasing the elasticity of the fluid by practically modifying the polymer concentration (i.e. decreasing β), smaller values of Re_c^* are found for which the flow returns to steady-symmetric state when approaching from “above”. More importantly it can be seen that the data points follow a linear trend, providing us with further confirmation that in region (I) of Fig. 8b, the dimensionless parameter Wi_{eff} collapses all data.

Fig. 10 demonstrates the behaviour of the FENE–MCR model for a fixed solvent-to-total viscosity ratio $\beta = 0.90$ when different values of the extensibility parameter L^2 are considered. The investigation of the influence of L^2 on the inertial instability is performed for decreasing ramps of Re at constant Wi numbers, similar to the investigation described in Section 4.3 for the cases of $\beta = 0.90$ and $\beta = 0.95$ with $L^2 = 5000$. In particular, Fig. 10a corresponds to the case with $L^2 = 2500$, while Fig. 10b and 10c demonstrate the responses for $L^2 = 1000$ and, $L^2 = 500$ respectively. Comparing the behaviours of the three different cases of Fig. 10, it is clear that polymer solutions consisting of molecules that have larger maximum extensibility lengths, are able to modify the flow field more and therefore, to maintain the flow destabilisation for smaller Reynolds numbers. As was shown in Section 2, the higher the value of L^2 the more elastic the fluid will be, with N_1 and n_e reaching higher plateau values for increasing shear rates and strain rates, respectively. The behaviours of all FENE–MCR fluids with $\beta = 0.90$ and different extensibility parameters are shown in Fig. 11, where the effective Weissenberg number is presented as a function of Re_c^* . It can be seen that the fluids exhibit a similar behaviour for very low elasticity values, but their responses start to deviate more significantly in region (I), compared to what was seen previously with all data collapsing (c.f. Section 4.3) within this region. This is clearly an effect of the L^2 parameter which is directly applied to the flow field

through the developed normal stresses and consequently through the first normal-stress difference. Increasing L^2 further is not expected to influence the flow field more, as verified by the inset of Fig. 11, where the variation of Re_c^* is given as a function of L^2 . Clearly any further increases of the extensibility will lead to a plateau for Re_c^* that corresponds to the Oldroyd-B limit ($L^2 \rightarrow \infty$).

4.5. Behaviour of first normal-stress differences

An interesting effect observed during this study is the behaviour of the first normal-stress difference, $N_1 = \tau_{xx} - \tau_{yy}$. Usually, numerical or experimental studies related to viscoelastic fluids in cross-slot geometries are performed under creeping ($Re \rightarrow 0$) or very low Re conditions, effectively enhancing elasticity. The majority of these studies focus mostly on investigating the stretching of polymeric chains and usually report the critical conditions and mechanisms for the onset of elastic instabilities, by exploiting the existence of the stagnation point [2,14,16,18–20,22,23,28,64,65]. For free stagnation point flows it is already known experimentally that when a specific characteristic Weissenberg number is achieved (i.e. $Wi_c \sim 0.5$), polymer chains are stretched while approaching the region of the stagnation point and form a sharp birefringent strand [18,24,64]. This thin strand is shaped along the outflow directions indicating significant stretching, high tensile stress differences and macromolecular orientation at the region close to the stagnation point, increasing in length and intensity as the flow rate (and thus Wi) is increased [2,14,18]. Numerically, this effect is evaluated by taking directly the difference between the normal stresses that are evaluated from the numerical simulations [19,20,22,23,64,65]. Poole et al. [19] investigated the flow of a viscoelastic fluid described by the UCM model within a 2D cross-slot

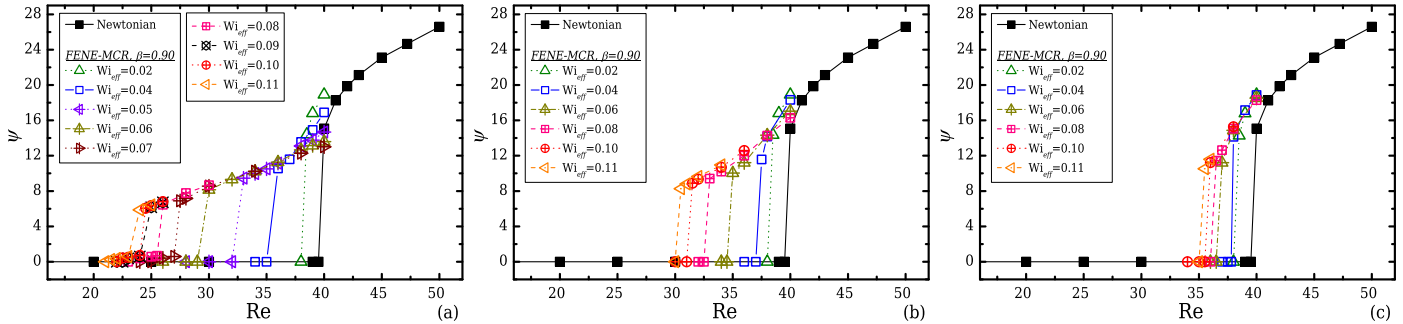


Fig. 10. Behaviour of the FENE–MCR fluids for $\beta = 0.90$ when (a) $L^2 = 2500$, (b) $L^2 = 1000$ and (c) $L^2 = 500$, at decreasing ramps of Re while Wi is constant. All three cases are compared to the response of the Newtonian fluid.

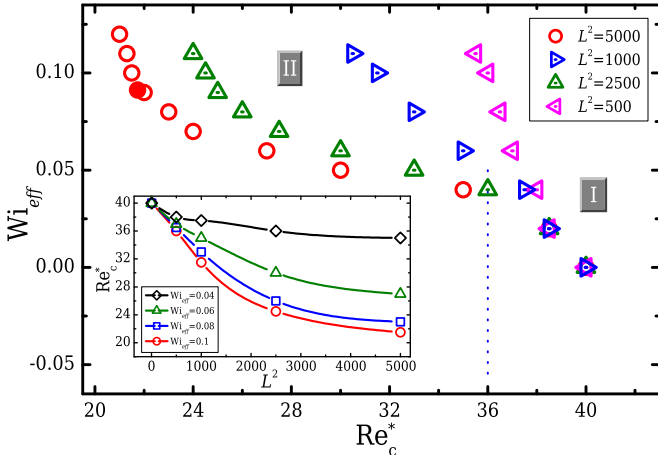


Fig. 11. Effective Weissenberg number as a function of Re_c^* for the FENE–MCR model with $\beta = 0.90$ when different values of L^2 are considered. The closed symbols correspond to the cases where El is constant, while the open symbols refer to the cases of constant Wi . The inset figure demonstrates the variation of Re_c^* as a function of L^2 .

geometry and reported the critical conditions for the onset of flow asymmetries due to elasticity. The authors demonstrated the growth of the birefringent strand with increasing Wi downstream of the stagnation point, and also compared this behaviour with the equivalent response of a Newtonian fluid under creeping flow conditions. Similarly, Xi and Graham [64] used a highly-elastic fluid described by the FENE-P model and illustrated a non-monotonic increase on the width of the birefringent strand in a 2D cross-slot with increasing elasticity. The authors correlated this response with the behaviour of the birefringent strand that was observed with dilute solutions in the opposed-jet experiments of Müller et al. [6]. Moreover, during the opposed-jet experiments by Müller et al. [6] an interesting oscillating behaviour of the width of the birefringent strand between two values was reported. The authors assumed that this behaviour was due to the loss of the stagnation point.

In Fig. 12 we present 3D contour-plots of the dimensionless first normal-stress difference, $N_1^* = N_1/(\eta U/w)$, with superimposed streamlines along the flow centreplanes for the Newtonian fluid, the UCM at constant elasticity $El = 0.00083$ and the FENE–MCR model with $\beta = 0.90$ and $L^2 = 5000$ at $El = 0.0042$, obtained from the decreasing Re ramps discussed in Section 4.1, 4.2. Starting from the case of the Newtonian fluid it can be seen that at $Re = 5$, displayed in Fig. 12a, N_1^* has the “expected” behaviour with the maximum values being at the stagnation point and slowly decaying along all directions, generating a “sphere-like” shape. At higher flow rates and when $Re = 39$ (still steady-symmetric flow), it can be seen from Fig. 12b that N_1^* obtains slightly higher values, while the region of influence acquires a more “bullet-like” shape and is evidently affected by the stronger inertia. When the flow is steady-asymmetric and the spiral vortex is formed, the behaviour of the first normal-stress difference is modified completely as shown in Fig. 12c. For this last case, N_1^* presents two regions of high values that are located some distance away from the vortex centrepoint (see inset figure of Fig. 12c).

Examining now the case of the UCM fluid at $El = 0.00083$ presented in Fig. 12d, it can be seen that for low Re , similar to the Newtonian case, the flow field is virtually unaffected by the polymer stress, with N_1^* exhibiting a Newtonian-like behaviour. For the case of Fig. 12e at $Re = 30.12$, Dean vortices are observed as expected, with the behaviour of the UCM fluid being again similar to the Newtonian case for $Re = 39$. The restrictions of the model discussed in Section 2 and the resulting low elasticity levels considered, lead to the conclusion that the flow field cannot be affected dramatically by the polymer, except from the already shown decrease of Re_c^* and the growth of ψ , being dominated by inertia forces. Equivalent observations can be made and when the flow

is steady-asymmetric, shown in Fig. 12f, where the dimensionless first normal-stress difference has, as in the Newtonian case, two peaks a certain distance from the vortex centrepoint.

Moving now to the case of the FENE–MCR fluid with $\beta = 0.90$ at $El = 0.0042$, it can be seen that a completely different response is manifested. When the flow is at low Re and Wi_{eff} , displayed in Fig. 12g, the thin strand of the first normal-stress difference is formed, indicating that for this particular case an extra tension is applied along the streamlines stretching the polymer molecules. The strand has higher values along the xy -centreplane at the region around the stagnation point and extends a distance downstream of the cross-slot centre. The width of the strand at this steady-symmetric state, decays along the vertical z -direction in a similar way to that shown by Cruz et al. [23] for a UCM fluid in a 3D cross-slot at $Re \rightarrow 0$. Interestingly, for higher values of Re and Wi_{eff} , and while the flow is still steady-symmetric, as shown in Fig. 12h, the form of the birefringent strand is modified and obtains a new structure. It can be seen that now the maximum high-stress values are located at off-centre vertical positions along the z -direction, directly “below” and “above” the stagnation point and not at the region around it (i.e. geometric centre location). At these off-centre positions, localised high stretching of the polymer chain occurs, extending spatially downstream of these locations. Finally for the steady-asymmetric flow shown in Fig. 12i, it can be seen that the maximum values of N_1^* are now located at the vortex core in contrast to the cases of the Newtonian and UCM fluids.

The results presented so far indicate a combination of inertial and elastic effects leads to very rich flow and stress fields. In Fig. 13 the response of N_1^* at various spatial locations as a function of Wi_{eff} is presented, for the cases of the FENE–MCR model with $\beta = 0.90$ and $\beta = 0.95$, during the constant elasticity number cases discussed in Section 4.2. For both cases N_1^* is reported at the geometric centrepoint for increasing and decreasing ramps. Starting from the case of $\beta = 0.90$ shown in Fig. 13a, it can be seen that for low values of Wi_{eff} , within the range $0 < Wi_{eff} < 0.03$, the dimensionless first normal-stress difference obtains its maximum value at the geometric centre of the domain (i.e. the stagnation point). As Wi_{eff} and subsequently Re increases, N_1^* starts to obtain higher values, compared to the centrepoint, some vertical distance along the z -direction from the stagnation point. The difference between the centrepoint and the off-centre values (symmetric locations bottom and top from the stagnation point) becomes larger as we approach the critical conditions for the inertial instability. Additionally, the trends for both values (centre and off-centre) present a non-monotonic behaviour. Finally, once the central spiral vortex is formed, the region of the highest N_1^* relocates to the vortex core as shown in Fig. 12i, in contrast to the Newtonian and the UCM cases. The transition to asymmetry at $Wi_{eff} \sim 0.09$ gives rise to a significant drop in the off-centre maxima. A similar response is observed for the case of $\beta = 0.95$ shown in Fig. 13b. It is noted that inertia is higher for the case of $\beta = 0.95$ and this partially explains the appearance of the off-centre N_1^* peaks at lower Wi_{eff} .

The existence of the off-centre N_1^* peaks and its non-monotonic behaviour for increasing pairs of Wi_{eff} and Re can be explained by the interplay between inertia and elasticity. Examining the streamlines and the dimensionless velocity magnitude in Fig. 14a, it is obvious that the flow can be considered as a quasi-2D flow at low Re (except close to the walls). Fluid elements approaching the middle of the cross-slot almost immediately turn towards the outlets of the configuration. As they approach the stagnation point region, they are highly stretched and then are oriented towards the outlets, generating the known form of the birefringent strand [23]. On the contrary, the flow field of Fig. 12h depicts a more complex situation than previously observed at low Re , due to inertia. Fluid elements that are now approaching the stagnation point are stretched, but then are directed towards the bottom and top walls of the configuration due to the existence of the Dean vortices. These bottom and top oriented fluid streams are forming new stagnation points, as can be seen in Fig. 14b, at the bottom and top walls and

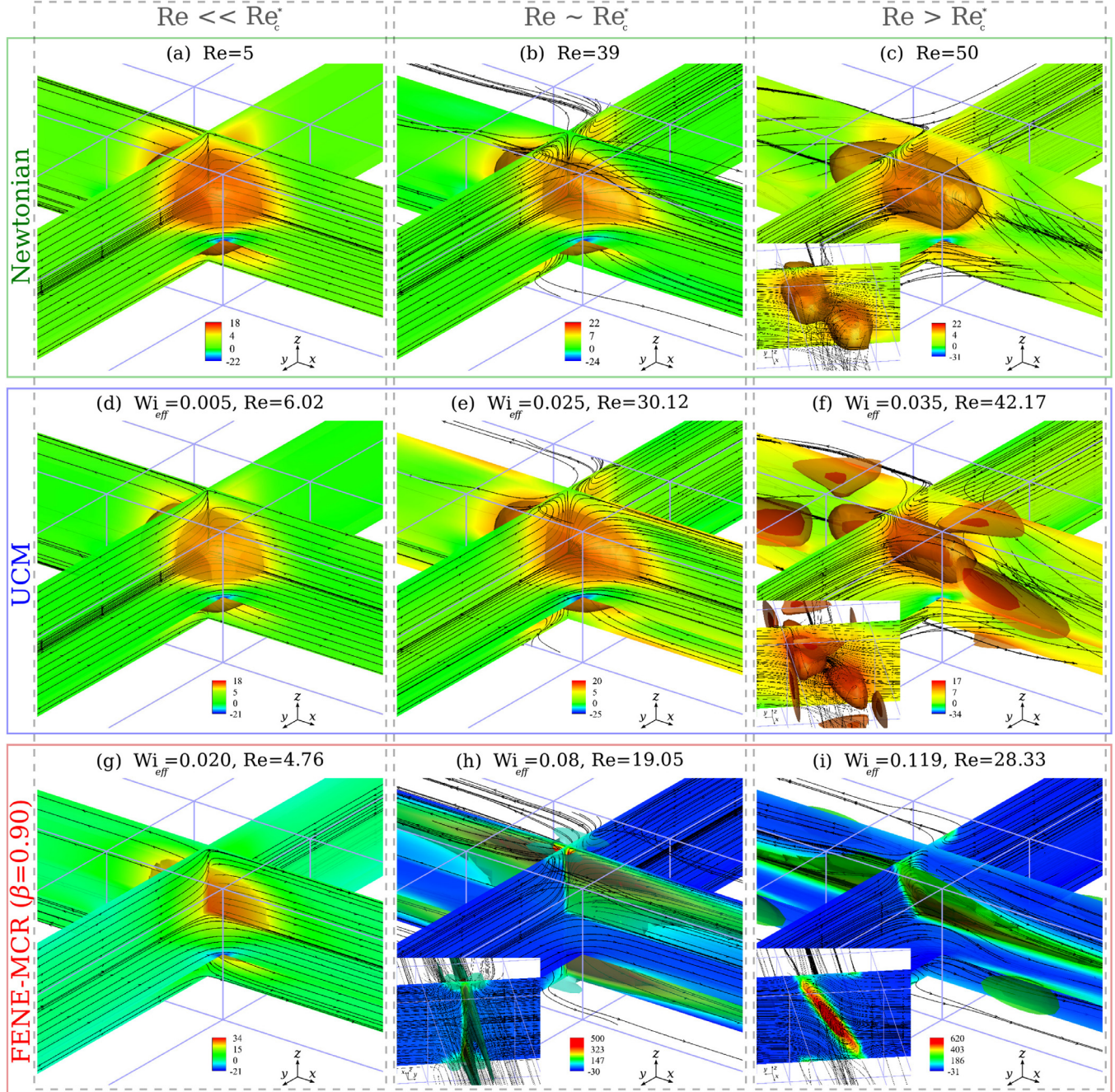


Fig. 12. Dimensionless first normal-stress difference, $N_1^* = N_1/(\eta U/w)$, contour-plots with superimposed streamlines along the flow centreplanes for (a-c) the Newtonian fluid, (d-f) the UCM at $\text{El} = 0.00083$ and (g-i) the FENE–MCR model at $\text{El} = 0.0042$ with $\beta = 0.90$ and $L^2 = 5000$. The inset figures of parts (c), (f), (h) and (i) correspond to the same 3D contour-plots from a different viewing angle. Figures (a-e) demonstrate the 3D isocontour at $N_1^* = 10$, (f) at $N_1^* = 10$ and $N_1^* = 15$, (g) at $N_1^* = 20$, (h) at $N_1^* = 320$ and $N_1^* = 100$ and (i) at $N_1^* = 500$ and $N_1^* = 250$.

together with the incoming streams from the inlets, are additionally stretching the fluid elements along this path generating this interesting behaviour of N_1^* . Moreover, additional stagnation points are created at the “core” of each Dean vortex, due to the incoming inlet streams and the outgoing fluid from the core of the cross-slot. Similar observations can be made when the flow is destabilised as shown in Fig. 14c. Considering the convection term of the upper-conveyed derivative ($\mathbf{u} \cdot \nabla \tau_p$), we can state that, since for an appropriate Wi_{eff} and Re the velocity component along the z -direction is no longer negligible in the vicinity of the stagnation point, stresses from the stretching history of the polymer are accumulated along the third direction. We believe this effect, together with the new stagnation points which contribute further to the extension of fluid elements, are responsible for the observed N_1^*

peaks. We are unable to observe this for the UCM, the FENE–MCR with $\beta = 0$ and the Oldroyd-B models, because the polymers are stretched at low elasticity values and their relaxation times are small enough, managing to relax and not to accumulate stresses. Thus, for the UCM and the Oldroyd-B models this is a direct consequence of being restricted to low Wi values for these models.

The non-monotonic behaviour of N_1^* is most likely occurring for the same reasons as was explained by Xi and Graham [64]. For faster incoming convective flows, more unstretched polymer molecules approach the stagnation point, which then have less time to become fully-stretched resulting in smaller values for N_1^* . Obviously, due to the hysteretic behaviour, this response is observed in different ranges for decreasing and for increasing ramps for both FENE–MCR fluids.

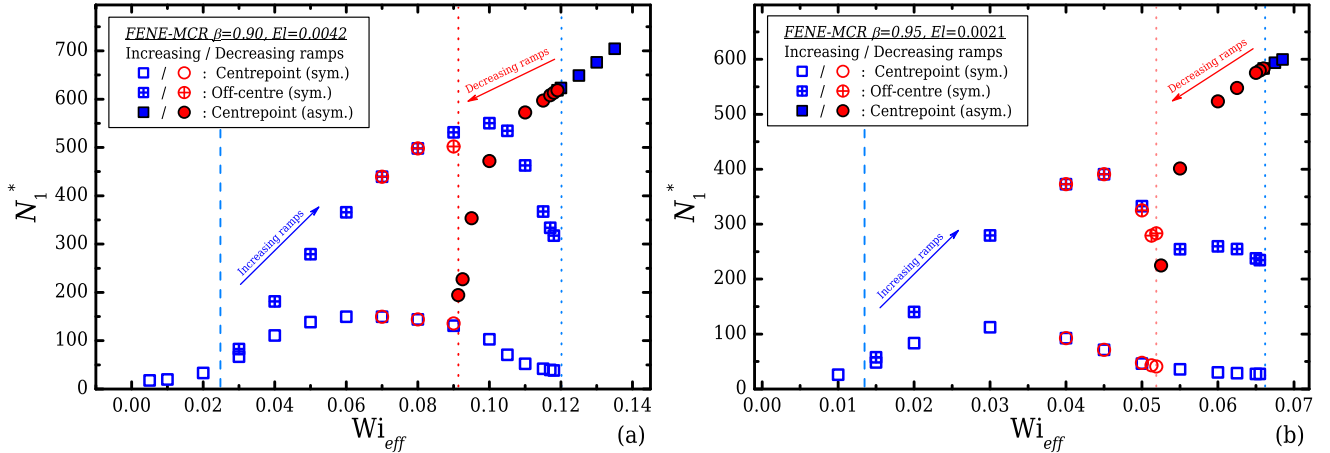


Fig. 13. Behaviour of the dimensionless first normal-stress differences, $N_1^* = N_1 / (\eta U / w)$, at the interrogation area for the FENE–MCR fluid with $L^2 = 5000$ for (a) $\beta = 0.90$ and (b) $\beta = 0.95$. Open symbols correspond to the values obtained at the centrepoint when the flow is steady-symmetric and closed symbols to the equivalent value when the flow is steady-asymmetric. The crossed-symbols depict the values obtained at the off-centre locations. The dashed and dotted lines are a guide to the eye, with the former pointing approximately the locations where the off-centre peaks start to form, while the latter indicate the locations where the state transitions occur for either increasing or decreasing Re ramps.

In order to further support these observations we examine the flow-type parameter ξ defined in Eq. (5) and introduced in Section 2. Fig. 15 demonstrates how the flow is classified for a Newtonian fluid and the FENE–MCR fluid with $\beta = 0.90$ at $El = 0.0042$. Starting from the low Re cases, in Fig. 15a for the Newtonian fluid and in Fig. 15d for the FENE–MCR model, it can be seen that both fluids illustrate a similar flow-type distribution. The flow at the inlets and the outlets is shear dominated, while the central part of geometry is essentially extensionally-dominated around the central stagnation point. When the flow is at higher Re values and the Dean vortices are formed, extension is increased at the top and bottom walls, precisely between each of the two counter-rotating Dean vortices as shown in Fig. 15b and 15e due to the two additional stagnation points. Further, for the FENE–MCR fluid, this stretching is also influenced by the streams meeting at the cores of the Dean vortices. Finally, when the flow is steady-asymmetric, the contours of the flow-type parameter in Fig. 15c indicate that there is a combination of rotation and shear around the vortex core. On the contrary, for the FENE–MCR model shown in Fig. 15f rotation is very small and the flow is mostly dominated by shear in the core.

5. Conclusions

An extensive numerical study on the effects of viscoelasticity upon the critical conditions and the characteristics of the inertial instability that is generated in a three-dimensional cross-slot with a square cross-section ($AR = 1$) was undertaken. Three viscoelastic models were

employed, namely the UCM, the Oldroyd-B and the FENE–MCR models. The use of the first two models was shown to be extremely limited, due to their inherent drawback of predicting infinite extensional viscosity above a critical Weissenberg number ($Wi_c = 0.5$) in steady-state extensional flows, as is the case investigated here at the free stagnation point. Our results demonstrate that the interplay between inertia and elastic forces result in a very rich flow where various behaviours and mechanisms can be observed.

Two different strategies were employed, one considering constant elasticity number flows and one where Wi is kept constant while Re is allowed to vary. All viscoelastic models in both strategies demonstrated a common behaviour, altering the critical conditions for the onset of the flow asymmetry. For all data sets, the critical Reynolds numbers (Re_c^*) were decreased compared to the case of a Newtonian fluid, both for increasing or decreasing ramps in Reynolds numbers. Additionally, the solutions provided by the viscoelastic models demonstrated a hysteretic behaviour between the increasing and decreasing ramps on the critical conditions of the flow transition, similar to the behaviour of the Newtonian fluid. Moreover it was shown that in the limit of $(Re_c^{*,N} - Re_c^*) / Re_c^{*,N} \ll 1$, our definition of Wi_{eff} manages to demonstrate a similar response for all fluids. On the contrary, for moderate elasticity values, the FENE–MCR model predicted solutions for the centerpoint vorticity at smaller values compared to the Newtonian case, similar to the experimental findings of Burshtein et al. [45], while in addition to this, Wi_{eff} clearly demonstrates a dependency on the β parameter (i.e. solvent-to-total viscosity ratio). These observations were further

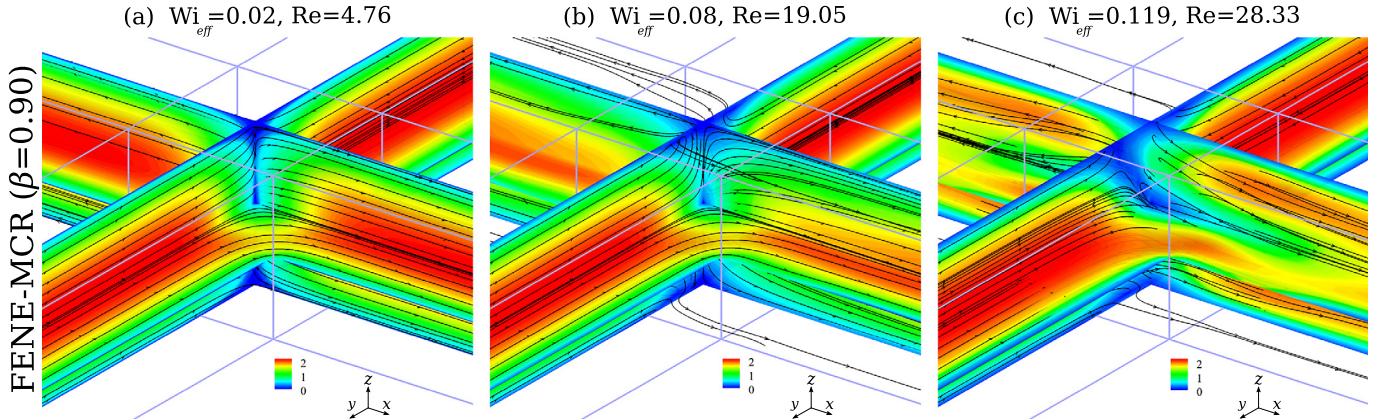


Fig. 14. Non-dimensional velocity magnitude $|u|/U$ contours with superimposed streamlines for the FENE–MCR fluid with $L^2 = 5000$ for $\beta = 0.90$ at $El = 0.0042$.

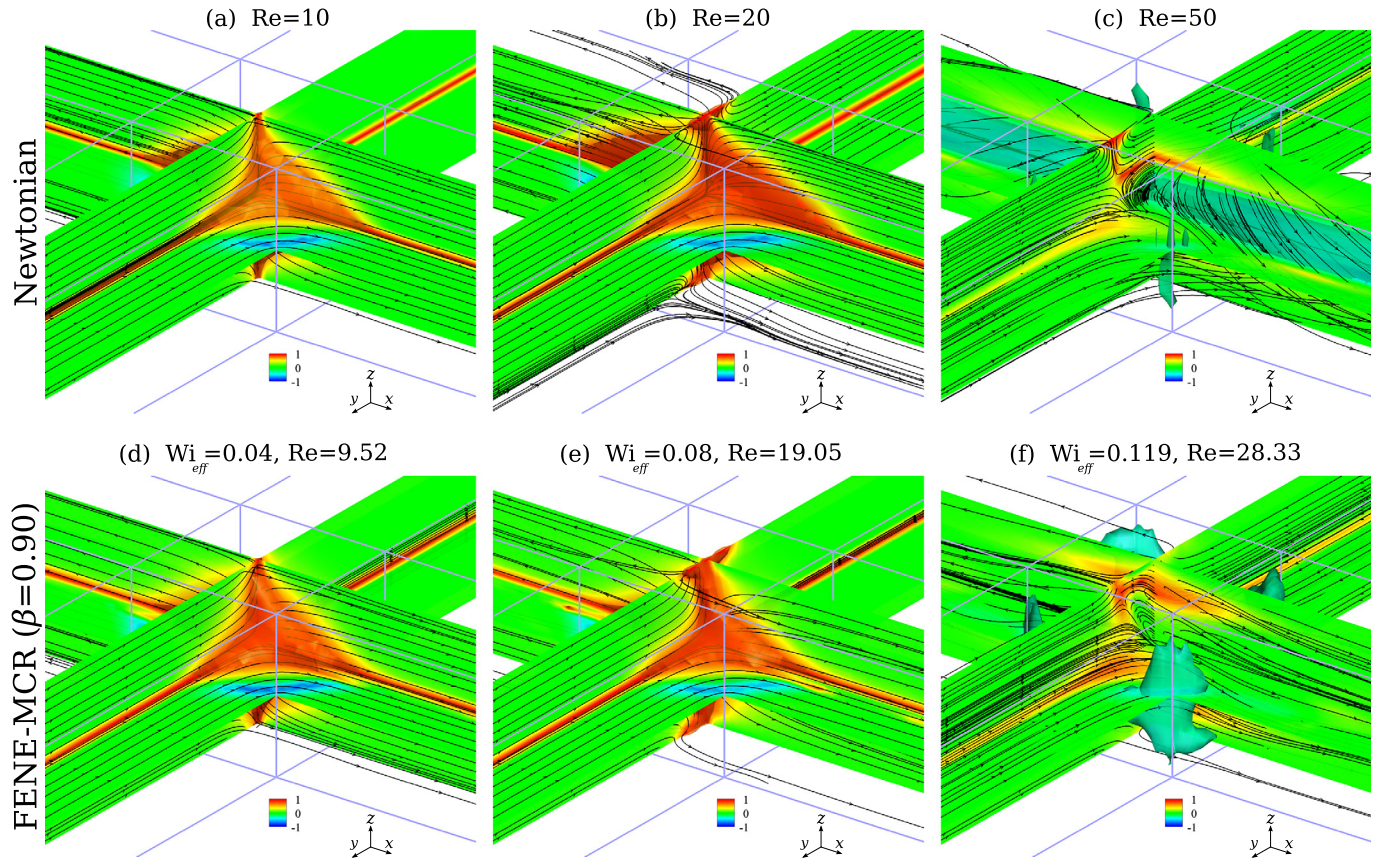


Fig. 15. Flow-type parameter contours with superimposed streamlines for (a-c) the Newtonian fluid and (d-f) the FENE-MCR model with $L^2 = 5000$ for $\beta = 0.90$ at $\text{El} = 0.0042$. (a,b,d,e) demonstrate the 3D isocontour at $\xi = 0.7$, (c,f) at $\xi = -0.5$.

supported since it was found that the characteristics of the inertial instability are affected by the choice of β and L^2 . In fact by modifying β one is actually changing the concentration of the polymer solution, while by changing the L^2 parameter one can alter the characteristics by just using a more extensible molecule. Moreover the investigation upon the influence of L^2 , demonstrates that the normal stresses and thus N_1 , are responsible for the flow destabilisation at lower Re_c^* .

The flow field at the moderate elasticity values is further modified by the interesting behaviour of the first normal-stress difference. Regions of high tensile-stresses were seen to be formed at off-centre locations away from the stagnation point. This effect is explained via the accumulation of stresses in additional directions and the existence of new stagnation points that are generated due to the highly 3D effects for increasing Re (i.e. Dean vortices) which results in new stretching regions. This corresponds to a different response from the already known birefringent strand that is formed around the stagnation point in a 2D flow. We believe that this is likely the cause of the flow destabilization at lower Reynolds numbers with lower centerpoint vorticity values compared to the Newtonian case. In contrast to this response, for the lower elasticity cases the behaviour of N_1^* was seen to be similar to the Newtonian case, with the centerpoint vorticity on the other hand obtaining higher values for the viscoelastic fluids.

The current study has focused only on the case with $\text{AR} = 1$. Although previous work has shown that AR can have a significant effect on the value of Re_c^* and on the type of the transition (about a tricritical point), we expect that the effect of elasticity on the resulting vortex will be qualitatively similar, regardless of AR . However, it would be of potential interest in future work to investigate any possible modifications on the type of the instability produced by shallower or deeper channels and also to examine how this parameter influences the behaviour of N_1 and the formation of stagnation points.

Concluding, studies that are related to inertial microfluidics could benefit from these results. For example the efficiency of mixing in a

microfluidic cross-slot geometry at lower Re could be investigated using low concentration polymer solutions. Additionally, research areas that focus on cell/sample deformations should be aware of the rich dynamics existing in these types of flows, such as the stress non-uniformity and the high tensile-stresses that develop far from the geometric centerpoint of the domain for $\text{Re} < \text{Re}_c^*$.

Acknowledgements

K. Z. and R. J. P. acknowledge funding from the EPSRC (UK) through Grant no. EP/M025187/1. N. B., S. J. H. and A. Q. S. gratefully acknowledge the support of Okinawa Institute of Science and Technology Graduate University, with subsidy funding from the Cabinet Office, Government of Japan. A. Q. S. and N. B. also acknowledge funding from the Japan Society for the Promotion of Science (Grants-in-Aid for Scientific Research (C) Grant No. 17K06173, and JSPS Research Fellow Grant No. 17J00412, respectively).

References

- [1] F.J. Galindo-Rosales, M.S.N. Oliveira, M.A. Alves, Microdevices for extensional rheometry of low viscosity elastic liquids: a review, *Microfluid. Nanofluid.* 14 (2013) 1–19, <http://dx.doi.org/10.1007/s10404-012-1028-1>.
- [2] S.J. Haward, Microfluidic extensional rheometry using stagnation point flow, *Biomicrofluidics* 10 (2016) (043401), <http://dx.doi.org/10.1063/1.4945604>.
- [3] G.I. Taylor, The formation of emulsions in definable fields of flow, *Proc. R. Soc. London Ser. A* 146 (1934) 501–523, <http://dx.doi.org/10.1098/rspa.1934.0169>.
- [4] G.G. Fuller, L.G. Leal, Flow birefringence of dilute polymer solutions in two-dimensional flows, *Rheol. Acta* 19 (1980) 580–600, <http://dx.doi.org/10.1007/BF01517512>.
- [5] P.N. Dunlap, L.G. Leal, Dilute polystyrene solutions in extensional flows: birefringence and flow modification, *J. Non Newton. Fluid Mech.* 23 (1987) 5–48, [http://dx.doi.org/10.1016/0377-0257\(87\)80009-5](http://dx.doi.org/10.1016/0377-0257(87)80009-5).
- [6] A.J. Müller, J.A. Odell, A. Keller, Elongational flow and rheology of monodisperse polymers in solution, *J. Non Newton. Fluid Mech.* 30 (1988) 99–118, [http://dx.doi.org/10.1016/0377-0257\(88\)80009-5](http://dx.doi.org/10.1016/0377-0257(88)80009-5).

- [org/10.1016/0377-0257\(88\)85018-3](http://dx.doi.org/10.1016/0377-0257(88)85018-3).
- [7] J.A. Odell, A. Keller, Y. Rabin, Flow-induced scission of isolated macromolecules, *J. Chem. Phys.* 88 (6) (1988) 4022–4028, <http://dx.doi.org/10.1063/1.453855>.
 - [8] R.R. Lagnado, L.G. Leal, Visualization of three-dimensional flow in a four-roll mill, *Exp. Fluids* 9 (1–2) (1990) 25–32, <http://dx.doi.org/10.1007/BF00575332>.
 - [9] V.N. Kalashnikov, M.G. Tsiklauri, Ordered three-dimensional structures resulting from instability of two-dimensional flow in crossed channels, *Fluid Dyn.* 26 (1991) 161–165, <http://dx.doi.org/10.1007/BF01050133>.
 - [10] V.N. Kalashnikov, M.G. Tsiklauri, Effect of polymer additives on ordered three-dimensional structures arising in cross-slot flow, *J. Non Newton. Fluid Mech.* 48 (1993) 215–223, [http://dx.doi.org/10.1016/0377-0257\(93\)87021-G](http://dx.doi.org/10.1016/0377-0257(93)87021-G).
 - [11] T.T. Perkins, D.E. Smith, S. Chu, Single polymer dynamics in an elongational flow, *Science* 276 (1997) 2016–2021, <http://dx.doi.org/10.1126/science.276.5321.2016>.
 - [12] D.E. Smith, S. Chu, Response of flexible polymers to a sudden elongation flow, *Science* 281 (1998) 1335–1340, <http://dx.doi.org/10.1126/science.281.5381.1335>.
 - [13] C.M. Schroeder, H.P. Babcock, E.S.G. Shaqfeh, S. Chu, Observation of polymer conformation hysteresis in extensional flow, *Science* 301 (2003) 1515–1519, <http://dx.doi.org/10.1126/science.1086070>.
 - [14] S.J. Haward, M.S.N. Oliveira, M.A. Alves, G.H. McKinley, Optimized cross-slot geometry for microfluidic extensional rheometry, *Phys. Rev. Lett.* 109 (128301) (2012), <http://dx.doi.org/10.1103/PhysRevLett.109.128301>.
 - [15] C.J. Pipe, G.H. McKinley, Microfluidic rheometry, *Mech. Res. Commun.* 36 (2009) 110–120, <http://dx.doi.org/10.1016/j.mechrescom.2008.08.009>.
 - [16] P.E. Arratia, C.C. Thomas, J. Diorio, J.P. Gollub, Elastic instabilities of polymer solutions in cross-channel flow, *Phys. Rev. Lett.* 96 (14) (2006) 144502, pRL. <https://doi.org/10.1103/PhysRevLett.96.144502>.
 - [17] S.J. Haward, G.H. McKinley, Instabilities in stagnation point flows of polymer solutions, *Phys. Fluids* 25 (083104) (2013), <http://dx.doi.org/10.1063/1.4818151>.
 - [18] S.J. Haward, T.J. Ober, M.S.N. Oliveira, M.A. Alves, G.H. McKinley, Extensional rheology and elastic instabilities of a wormlike micellar solution in a microfluidic cross-slot device, *Soft Matter* 8 (2012) 536–555, <http://dx.doi.org/10.1039/csm06494k>.
 - [19] R.J. Poole, M.A. Alves, P.J. Oliveira, Purely elastic flow asymmetries, *Phys. Rev. Lett.* 99 (2007) (164503), <http://dx.doi.org/10.1103/PhysRevLett.99.164503>.
 - [20] G.N. Rocha, R.J. Poole, M.A. Alves, P.J. Oliveira, On extensibility effects in the cross-slot flow bifurcation, *J. Non Newton. Fluid Mech.* 156 (2009) 58–69, <http://dx.doi.org/10.1016/j.jnnfm.2008.06.008>.
 - [21] A.M. Afonso, P.J. Oliveira, F.T. Pinho, M.A. Alves, Dynamics of high-deborah-number entry flows: a numerical study, *J. Fluid Mech.* 677 (2011) 272–304, <http://dx.doi.org/10.1017/jfm.2011.84>.
 - [22] F.A. Cruz, R.J. Poole, A.M. Afonso, F.T. Pinho, P.J. Oliveira, M.A. Alves, A new viscoelastic benchmark flow: stationary bifurcation in a cross-slot, *J. Non Newton. Fluid Mech.* 214 (2014) 57–68, <http://dx.doi.org/10.1016/j.jnnfm.2014.09.015>.
 - [23] F.A. Cruz, R.J. Poole, A.M. Afonso, F.T. Pinho, P.J. Oliveira, M.A. Alves, Influence of channel aspect ratio on the onset of purely-elastic flow instabilities in three-dimensional planar cross-slots, *J. Non Newton. Fluid Mech.* 227 (2016) 65–79, <http://dx.doi.org/10.1016/j.jnnfm.2015.11.008>.
 - [24] J.A. Pathak, S.D. Hudson, Rheo-optics of equilibrium polymer solutions: wormlike micelles in elongational flow in a microfluidic cross-slot, *Macromolecules* 39 (2006) 8782–8792, <http://dx.doi.org/10.1021/ma061355r>.
 - [25] S.J. Haward, A. Jaishankar, M.S.N. Oliveira, M.A. Alves, G.H. McKinley, Extensional flow of hyaluronic acid solutions in an optimized microfluidic cross-slot device, *Biomicrofluidics* 7 (044108), 2013. <https://doi.org/10.1063/1.4816708>.
 - [26] V. Sharma, S.J. Haward, J. Serdy, B. Keshavarz, A. Soderlund, P. Threlfall-Holmes, G.H. McKinley, The rheology of aqueous solutions of ethyl hydroxy-ethyl cellulose (EHEC) and its hydrophobically modified analogue (hmEHEC): extensional flow response in capillary break-up, jetting (ROJER) and in a cross-slot extensional rheometer, *Soft Matter* 11 (2015) 3251–3270, <http://dx.doi.org/10.1039/C4SM01661K>.
 - [27] M.A. Alves, Design a cross-slot flow channel for extensional viscosity measurements, *AIP Conf Proc.* 1027 (2008), pp. 240–242.
 - [28] F.J. Galindo-Rosas, M.S.N. Oliveira, M.A. Alves, Optimized cross-slot micro-devices for homogeneous extension, *RSC Adv.* 4 (2014) 7799–7804, <http://dx.doi.org/10.1039/c3ra47230b>.
 - [29] D.R. Gossett, H.T.K. Tse, S.A. Lee, Y. Ying, A.G. Lindgren, O.O. Yang, J. Rao, A.T. Clark, D.D. Carlo, Hydrodynamic stretching of single cells for large population mechanical phenotyping, *Proc. Natl. Acad. Sci. U.S.A.* 109 (2012) 7630–7635, <http://dx.doi.org/10.1073/pnas.1200107109>.
 - [30] R. Dylla-Spears, J.E. Townsend, L. Jen-Jacobson, L.L. Sohn, S.J. Muller, Single-molecule sequence detection via microfluidic planar extensional flow at a stagnation point, *Lab Chip* (2010) 1543–1549, <http://dx.doi.org/10.1039/b926847b>.
 - [31] S. Cha, T. Shin, S.S. Lee, W. Shim, G. Lee, S.J. Lee, Y. Kim, J.M. Kim, Cell stretching measurement utilizing viscoelastic particle focusing, *Anal. Chem.* 84 (2012) 10471–10477, <http://dx.doi.org/10.1021/ac302763n>.
 - [32] M. Tanyeri, E.M. Johnson-Chavarria, C.M. Schroeder, Hydrodynamic trap for single particles and cells, *Appl. Phys. Lett.* 96 (2010) (224101), <http://dx.doi.org/10.1063/1.3431664>.
 - [33] M. Tanyeri, M. Ranka, N. Sittipolkul, C.M. Schroeder, A microfluidic-based hydrodynamic trap: design and implementation, *Lab Chip* 11 (10) (2011) 1786–1794, <http://dx.doi.org/10.1039/c0lc00709a>.
 - [34] M. Tanyeri, C.M. Schroeder, Manipulation and confinement of single particles using fluid flow, *Nano Lett.* 13 (2013) 2357–2364, <http://dx.doi.org/10.1021/nl4008437>.
 - [35] H. Amini, W. Lee, D.D. Carlo, Inertial microfluidic physics, *Lab Chip* 14 (2014) 2739–2761, <http://dx.doi.org/10.1039/c4lc00128a>.
 - [36] N. Nivedita, P. Ligurni, I. Papautsky, Dean flow dynamics in low-aspect ratio spiral microchannels, *Sci. Rep.-UK* 7 (2017) (44072), <http://dx.doi.org/10.1038/srep44072>.
 - [37] M.S.N. Oliveira, M.A. Alves, F.T. Pinho, Microfluidic Flows of Viscoelastic Fluids, in: R. Grigoriev (Ed.), *Transport and Mixing in Laminar Flows: From Microfluidics to Oceanic Currents*, Wiley-VCH Verlag GmbH & Co. KGaA, Weinheim, Germany, 2012. <https://doi.org/10.1002/9783527639748.ch6>
 - [38] N.T. Nguyen, *Micromixers*, (second ed.), William Andrew Publishing, 2012.
 - [39] S.J. Haward, R.J. Poole, M.A. Alves, P.J. Oliveira, N. Goldenfeld, A.Q. Shen, Tricritical spiral vortex instability in cross-slot flow, *Phys. Rev. E* 93 (2016) (031101), <http://dx.doi.org/10.1103/PhysRevE.93.031101>.
 - [40] W. Dean, LXII. The stream-line motion of fluid in a curved pipe (second paper), *Philos. Mag.* 5 (30) (1928) 673–695.
 - [41] R.J. Poole, M. Alfateh, A.P. Gauntlett, Bifurcation in a T-channel junction: effects of aspect ratio and shear-thinning, *Chem. Eng. Sci.* 104 (2014) 839–848, <http://dx.doi.org/10.1016/j.ces.2013.10.006>.
 - [42] N.A. Mouheb, A. Montillet, C. Solliec, J. Havlicka, P. Legentilhomme, J. Comiti, J. Thibon, Flow characterization in t-shaped and cross-shaped micromixers, *Microfluid. Nanofluid.* 10 (2011) 1185–1197, <http://dx.doi.org/10.1007/s10404-010-0746-5>.
 - [43] N.A. Mouheb, D. Malsch, A. Montillet, C. Solliec, T. Henkel, Numerical and experimental investigations of mixing in t-shaped and cross-shaped micromixers, *Chem. Eng. Sci.* 68 (2012) 278–289, <http://dx.doi.org/10.1016/j.ces.2011.09.036>.
 - [44] W.M. Abed, A.F. Domingues, R.J. Poole, D.J.C. Dennis, Heat transfer enhancement in a cross-slot micro-geometry, *Int. J. Therm. Sci.* 121 (2017) 249–265, <http://dx.doi.org/10.1016/j.ijthermalsci.2017.07.017>.
 - [45] N. Burshtein, K. Zografas, A.Q. Shen, R.J. Poole, S.J. Haward, Inertioelastic flow instability at a stagnation point, *Phys. Rev. X* 7 (041039) (2017), <http://dx.doi.org/10.1103/PhysRevX.7.041039>.
 - [46] M.D. Chilcott, J.M. Rallison, Creeping flow of dilute polymer solutions past cylinders and spheres, *J. Non Newton. Fluid Mech.* 29 (1988) 381–432, [http://dx.doi.org/10.1016/0377-0257\(88\)85062-6](http://dx.doi.org/10.1016/0377-0257(88)85062-6).
 - [47] P.J. Coates, R.C. Armstrong, R.A. Brown, Calculation of steady state viscoelastic flow through axisymmetric contractions with the EEME formulation, *J. Non Newton. Fluid Mech.* 42 (1992) 141–188, [http://dx.doi.org/10.1016/0377-0257\(92\)80008-L](http://dx.doi.org/10.1016/0377-0257(92)80008-L).
 - [48] P.S. Virk, H. Baher, The effect of polymer concentration on drag reduction, *Chem. Eng. Sci.* 25 (1970) 1183–1189, [http://dx.doi.org/10.1016/0009-2509\(70\)85008-4](http://dx.doi.org/10.1016/0009-2509(70)85008-4).
 - [49] K. Kim, C.F. Li, R. Sureshkumar, S. Balachandar, R.J. Adrian, Effects of polymer stresses on eddy structures in drag-reduced turbulent channel flow, *J. Fluid Mech.* 584 (2007) 281–299, <http://dx.doi.org/10.1017/S0022112007006611>.
 - [50] D. Samanta, Y. Dubief, M. Holzner, C. Schäfer, A.N. Morozov, C. Wagner, B. Hof, Elasto-inertial turbulence, *P. Natl. Acad. Sci. USA* 110 (2013) 10557–10562, <http://dx.doi.org/10.1073/pnas.1219661110>.
 - [51] M.D. Graham, Drag reduction and the dynamics of turbulence in simple and complex fluids, *Phys. Fluids* 26 (2014) (101301), <http://dx.doi.org/10.1063/1.4895780>.
 - [52] R.B. Bird, R.C. Armstrong, O. Hassager, *Dynamics of Polymeric Liquids*, John Wiley & Sons, New York, 1987. Volume 1: Fluid Dynamics
 - [53] J.H. Ferzinger, M. Perić, *Computational Methods for Fluid Dynamics*, Springer Berlin Heidelberg, 2002.
 - [54] R.G. Owens, T.N. Phillips, *Computational Rheology*, Imperial College Press, 2002.
 - [55] J.M. Rallison, E.J. Hinch, Do we understand the physics in the constitutive equation, *J. Non Newton. Fluid Mech.* 29 (1988) 37–55, [http://dx.doi.org/10.1016/0377-0257\(88\)85049-3](http://dx.doi.org/10.1016/0377-0257(88)85049-3).
 - [56] P.J. Oliveira, Asymmetric flows of viscoelastic fluids in symmetric planar expansion geometries, *J. Non Newton. Fluid Mech.* 114 (2003) 33–63, [http://dx.doi.org/10.1016/S0377-0257\(03\)00117-4](http://dx.doi.org/10.1016/S0377-0257(03)00117-4).
 - [57] A. Morozov, S.E. Spagnolie, Introduction to complex Fluids, in: S. Spagnolie (Ed.), *Complex Fluids in Biological Systems. Biological and Medical Physics, Biomedical Engineering*, Springer, New York, NY, 2015, pp. 3–52, , http://dx.doi.org/10.1007/978-1-4939-2065-1_1.
 - [58] P.J. Oliveira, F.T. Pinho, G.A. Pinto, Numerical simulation of non-linear elastic flows with a general collocated finite-volume method, *J. Non Newton. Fluid Mech.* 79 (1998) 1–43, [http://dx.doi.org/10.1016/S0377-0257\(98\)00082-2](http://dx.doi.org/10.1016/S0377-0257(98)00082-2).
 - [59] P.J. Oliveira, Method for time-dependent simulations of viscoelastic flows: vortex shedding behind cylinder, *J. Non Newton. Fluid Mech.* 101 (2001) 113–137, [http://dx.doi.org/10.1016/S0377-0257\(01\)00146-X](http://dx.doi.org/10.1016/S0377-0257(01)00146-X).
 - [60] M.A. Alves, P.J. Oliveira, F.T. Pinho, A convergent and universally bounded interpolation scheme for the treatment of advection, *Int. J. Numer. Meth. Fluids* 41 (2003) 47–75, <http://dx.doi.org/10.1002/fld.428>.
 - [61] J.S. Lee, R. Dylla-Spears, N.P. Teclamariam, S.J. Muller, Microfluidic four-roll mill for all flow types, *Appl. Phys. Lett.* 90 (2007) (074103), <http://dx.doi.org/10.1063/1.2472528>.
 - [62] J. Dealy, Weissenberg and Deborah numbers - their definition and use, *Rheol. Bull.* 79 (2010) 14–18.
 - [63] R.J. Poole, The Deborah and Weissenberg numbers, *Rheol. Bull.* 53 (2012) 32–39.
 - [64] L. Xi, M.D. Graham, A mechanism for oscillatory instability in viscoelastic cross-slot flow, *J. Fluid Mech.* 622 (2009) 145–165, <http://dx.doi.org/10.1017/S002211200805119>.
 - [65] A.M. Afonso, M.A. Alves, F.T. Pinho, Purely elastic instabilities in three-dimensional cross-slot geometries, *J. Non Newton. Fluid Mech.* 165 (2010) 743–751, <http://dx.doi.org/10.1016/j.jnnfm.2010.03.010>.